A QCTO-SI Approach for the Synthesis of Miniaturized Linear Conformal Arrays

M. Salucci, G. Oliveri, N. Anselmi, and A. Massa

Abstract

This work presents a novel material-by-design (*MbD*) technique aimed at synthesizing conformal and miniaturized linear arrays. A two-step quasi-conformal transformation (*QCTO*) approach is exploited in order to synthesize meta-material coverings of the conformal arrangements in order to restore their reference free-space radiation features. Moreover, a source inversion (*SI*) strategy is applied in order to reduce the number of radiators, by synthesizing a new set of excitations of the final conformal architecture. Some numerical results are presented in order to assess the effectiveness as well as the current limitations of the proposed *MbD* synthesis methodology.

1 Test "Circular-Arc-Spline" Geometry - $N' = 20$ ($s = 2.0[\lambda], l = 2.0[\lambda]$)

Input Parameters

- **Virtual & Physical Geometries**
  - The physical geometry is given by:
    - $-w_c/2 \leq x \leq w_c/2$: portion of circular arc passing through the points $(-w/2, 0.0)$, $(0.0, h)$ and $(w/2, 0.0)$;
    - $-w/2 \leq x < -w_c/2$: spline with $Q = 5$ control points (points A, B and C can be controlled);
    - $w_c/2 \leq x < w/2$: spline with $Q = 5$ control points (points D, E and F can be controlled);
  - The upper part of the virtual geometry is an exact copy of the physical one.

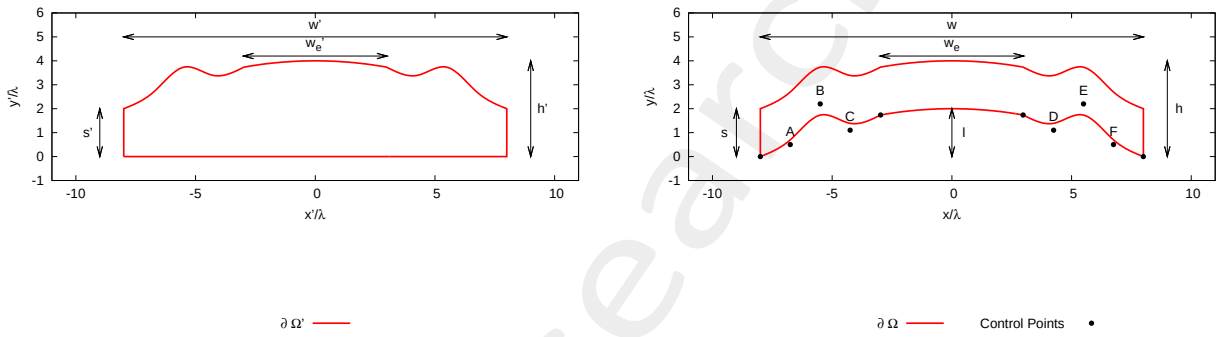

(a) VIRTUAL (b) PHYSICAL

Figure 1: Transformation regions and geometric parameters of interest.

- Width: $w = w' = 16.0$ $[\lambda]$;
- Extension of the circular arcs: $w_c = w_c'$ (see table below);
- Lens thickness: $s = s' = 2.0$ $[\lambda]$;
- Lens curvature: $l = 2.0[\lambda]$;
- Lens total height: $h = h' = l + s = 4.0$ $[\lambda]$;

	Left Spline			Right Spline			Circular arc
SYMMETRIC GEOMETRIES							
TEST CASE	y_A $[\lambda]$	y_B $[\lambda]$	y_C $[\lambda]$	y_D $[\lambda]$	y_E $[\lambda]$	y_F $[\lambda]$	$w_c = w_c'$ $[\lambda]$
1	0.5	2.2	**1.5**	**1.5**	2.2	0.5	**8.0**
2	0.5	2.2	**1.5**	**1.5**	2.2	0.5	**6.0**
3	0.5	2.2	**1.1**	**1.1**	2.2	0.5	**8.0**
4	0.5	2.2	**1.1**	**1.1**	2.2	0.5	**6.0**
ASYMMETRIC GEOMETRIES							
TEST CASE	y_A $[\lambda]$	y_B $[\lambda]$	y_C $[\lambda]$	y_D $[\lambda]$	y_E $[\lambda]$	y_F $[\lambda]$	$w_c = w_c'$ $[\lambda]$
5	0.5	2.2	**1.1**	**2.2**	**1.5**	0.5	**8.0**
6	0.5	2.2	**1.1**	**2.2**	**1.5**	0.5	**6.0**

Table I: y-coordinate of the control points for the lower spline and widths of the two circular arcs.

- **Virtual Array**
  - Number of elements, spacing, aperture: $N' = 20$, $d' = \frac{\lambda}{2}$, $L' = 9.5$ $[\lambda]$;
  - Distance from PEC ground plane (placed at $y' = 0.0$): $\delta' = \frac{\lambda}{4}$;
  - Operating frequency: $f = 600$ $[MHz]$;
  - Steering angle: $\phi_s = 90.0$ $[deg]$;
  - Excitations: $I_n = 1.0$, $\varphi_n = \frac{-2\pi}{\lambda} x_n sin\,(\phi_s + 90)$; $n = 1, ..., N'$;
- **QCTO**
  - Discretization cell dimension: 0.15 $[\lambda]$ (0.01 $[\lambda]$ for source mapping);

1.0.1 Results of the Transformation - Symmetric Test Cases

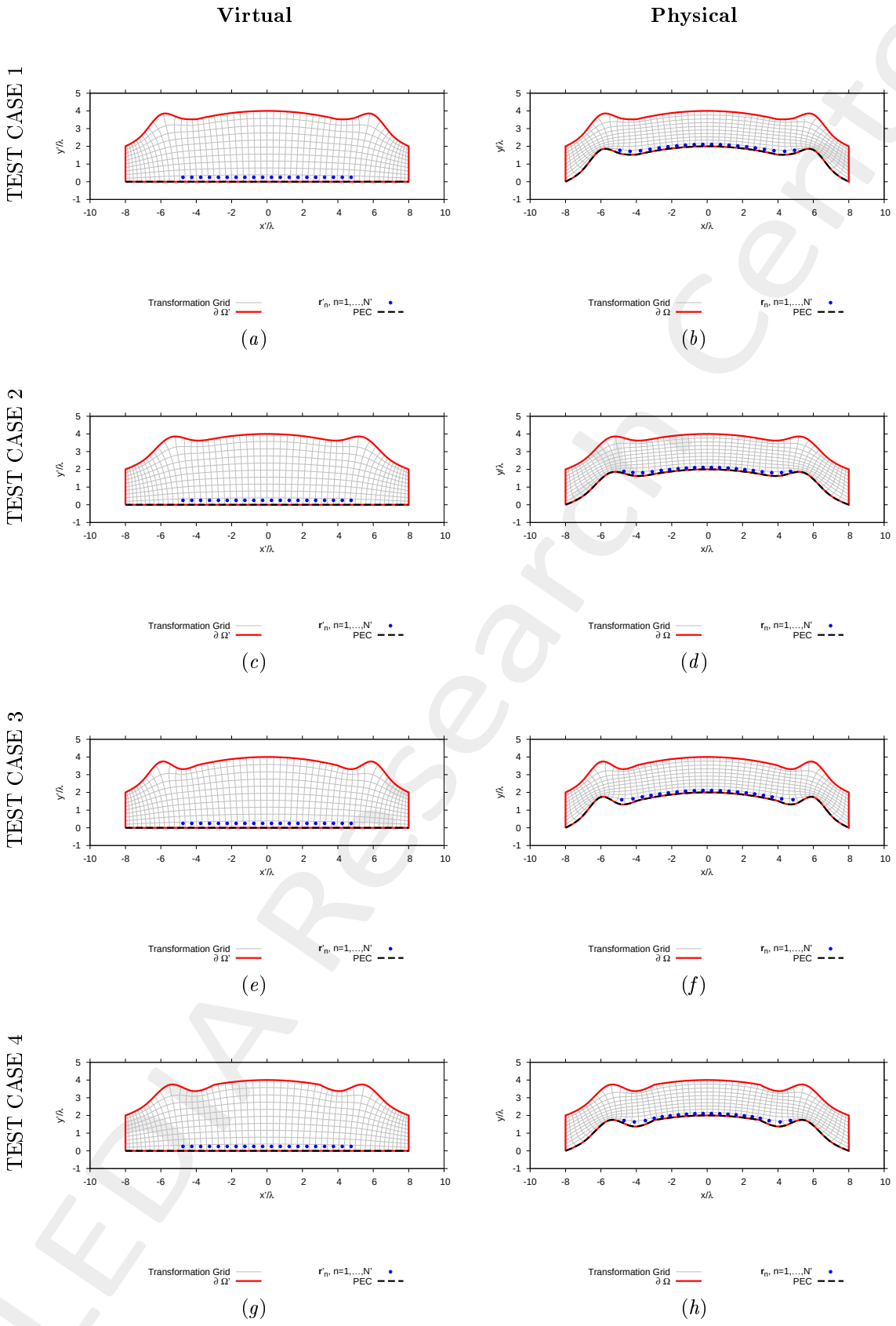

Figure 2: Transformation grids for virtual and physical geometries for different configurations of the lens.

1.0.2 Results of the Transformation - Asymmetric Test Cases

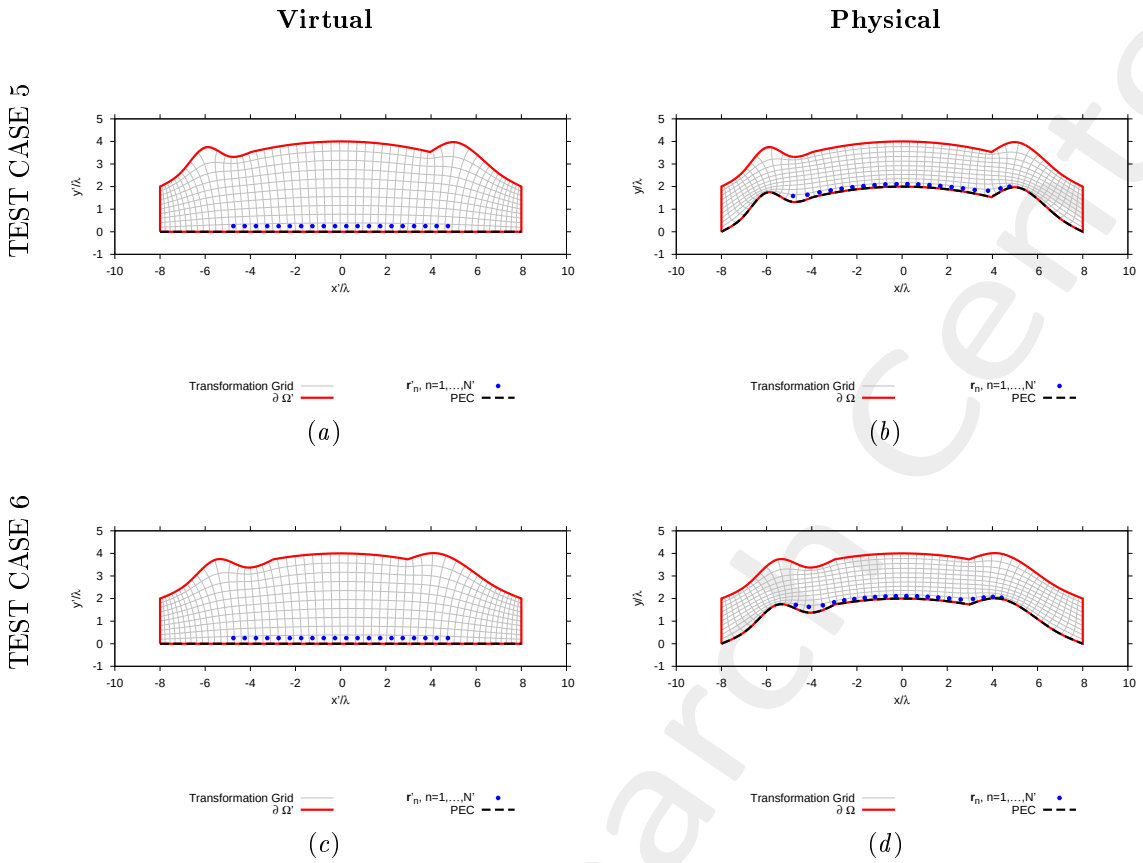

Figure 3: Transformation grids for virtual and physical geometries for different configurations of the lens.

1.0.3 Physical Lens Parameters

	SYMMETRIC				ASYMMETRIC	
	TEST CASE 1	TEST CASE 2	TEST CASE 3	TEST CASE 4	TEST CASE 5	TEST CASE 6
Anisotropic Permittivity Range	$[-4.37, 35.78]$	$[-1.64, 10.48]$	$[-6.76, 61.26]$	$[-1.76, 13.20]$	$[-1.55, 46.91]$	$[-1.00, 11.96]$
Isotropic Permittivity Range	$[0.00, 3.83]$	$[0.00, 3.23]$	$[0.00, 3.74]$	$[0.00, 3.17]$	$[0.00, 3.73]$	$[0.00, 3.16]$

Table II: Permittivity ranges of the physical lens.

1.0.4 Far-Field Patterns (Aniso-Lens, $\phi_s = 90.0$ [deg]) - Symmetric Test Cases

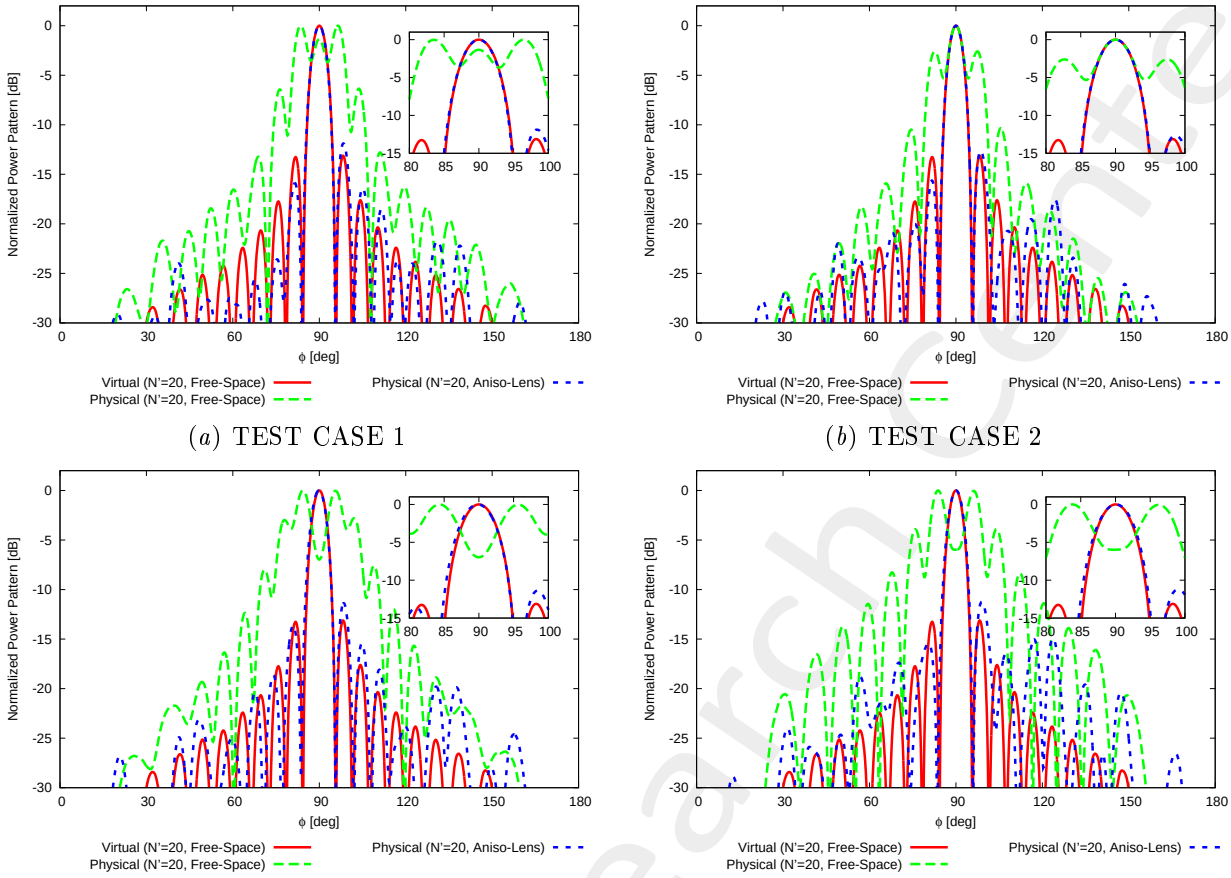

(a) TEST CASE 1 (b) TEST CASE 2

(c) TEST CASE 3 (d) TEST CASE 4

Figure 4: Comparison between the far field patterns.

1.0.5 Far-Field Patterns (Aniso-Lens, $\phi_s = 90.0$ [deg]) - Asymmetric Test Cases

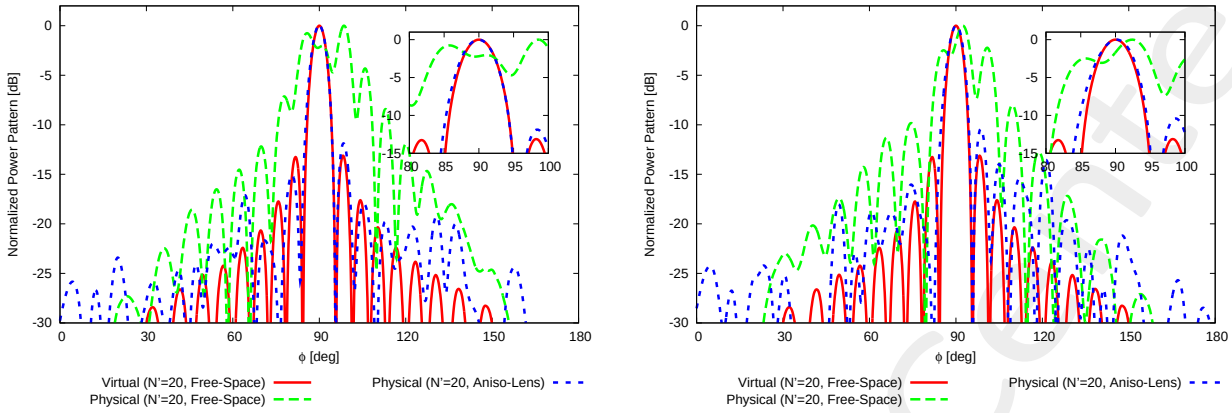

(*a*) TEST CASE 5 (*b*) TEST CASE 6

Figure 5: Comparison between the far field patterns.

2 "Circular-Arc-Low-Spline" Geometry - $N' = 20$ (With Compression) #1

Input Parameters

- **Virtual & Physical Geometries**

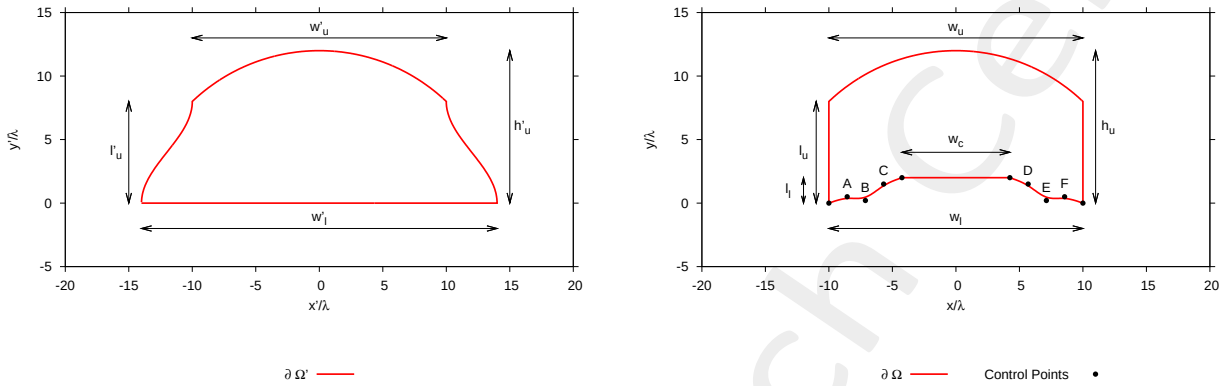

(*a*) **VIRTUAL** (*b*) **PHYSICAL (LENS)**

Figure 6: Transformation regions and geometric parameters of interest.

	VIRTUAL					PHYSICAL (LENS)												
TEST CASE	N'	w_l' [λ]	w_u' [λ]	h_u' [λ]	l_u' [λ]	N	w_l [λ]	w_u [λ]	h_u [λ]	l_u [λ]	l_l [λ]	w_c [λ]	y_A [λ]	y_B [λ]	y_C [λ]	y_D [λ]	y_E [λ]	y_F [λ]
1	20	**19.3**	20.0	12.0	8.0	**18**	20.0	20.0	12.0	8.0	2.0	8.5	0.5	0.2	1.5	1.5	0.2	0.5
2	20	**21.3**	20.0	12.0	8.0	**17**	20.0	20.0	12.0	8.0	2.0	8.5	0.5	0.2	1.5	1.5	0.2	0.5
3	20	**24.0**	20.0	12.0	8.0	**16**	20.0	20.0	12.0	8.0	2.0	8.5	0.5	0.2	1.5	1.5	0.2	0.5
4	20	**28.0**	20.0	12.0	8.0	**15**	20.0	20.0	12.0	8.0	2.0	8.5	0.5	0.2	1.5	1.5	0.2	0.5

Table III: Executed test cases. Objective: increase $w_l^{'}$ in order to obtain larger compressions of the original virtual array.

IMPORTANT NOTE: The minimum compression is for $N = 18$ ($L = 8.5$ [λ]) because this is the length of the linear segment in the physical lens (i.e., $w_c = 8.5[\lambda]$) on which the compressed array must stay.

- **Virtual Array**
  - Number of elements, spacing, aperture: $N' = 20$, $d' = \frac{\lambda}{2}$, $L' = 9.5$ [λ];
  - Distance from PEC ground plane (placed at $y' = 0.0$): $\delta' = \frac{\lambda}{4}$;
  - Operating frequency: $f = 600$ [MHz];
  - Excitations for steering at $\phi = \phi_s$: $I_n = 1.0$, $\varphi_n = \frac{-2\pi}{\lambda} x_n sin\,(\phi_s + 90)$; $n = 1, ..., N'$;
- **QCTO**
  - Discretization cell dimension: 0.15 [λ] (0.01 [λ] for source mapping);

2.0.6 Results of the Transformation

Compression of the virtual array

	VIRTUAL			PHYSICAL (LENS)	
TEST CASE	N'	L' $[\lambda]$	$w_l^{'}$ $[\lambda]$	N_{dense}	$L_{dense}[\lambda]$
1	20	9.5	19.3	20	8.52
2	20	9.5	21.3	20	8.00
3	20	9.5	24.0	20	7.50
4	20	9.5	28.0	20	7.05

Table IV: Number of elements and aperture of the array after compression from virtual to physical.

Physical lens parameters

	$w_l^{'} = 19.3$ $[\lambda]$	$w_l^{'} = 21.3$ $[\lambda]$	$w_l^{'} = 24.0$ $[\lambda]$	$w_l^{'} = 28.0$ $[\lambda]$
Anisotropic Permittivity Range	$[-0.82, 3.65]$	$[-0.77, 3.81]$	$[-0.73, 4.44]$	$[-0.66, 6.21]$
Isotropic Permittivity Range	$[0.00, 3.62]$	$[0.00, 4.62]$	$[0.00, 6.18]$	$[0.00, 8.16]$
Average Fractional Anisotropy, α_F	2.46×10^{-1}	2.35×10^{-1}	2.41×10^{-1}	2.66×10^{-1}
Average Relative Anisotropy, α_R	2.18×10^{-1}	2.09×10^{-1}	2.17×10^{-1}	2.47×10^{-1}

Table V: Permittivity ranges and anisotropy measures of the physical lens.

Transformation grids

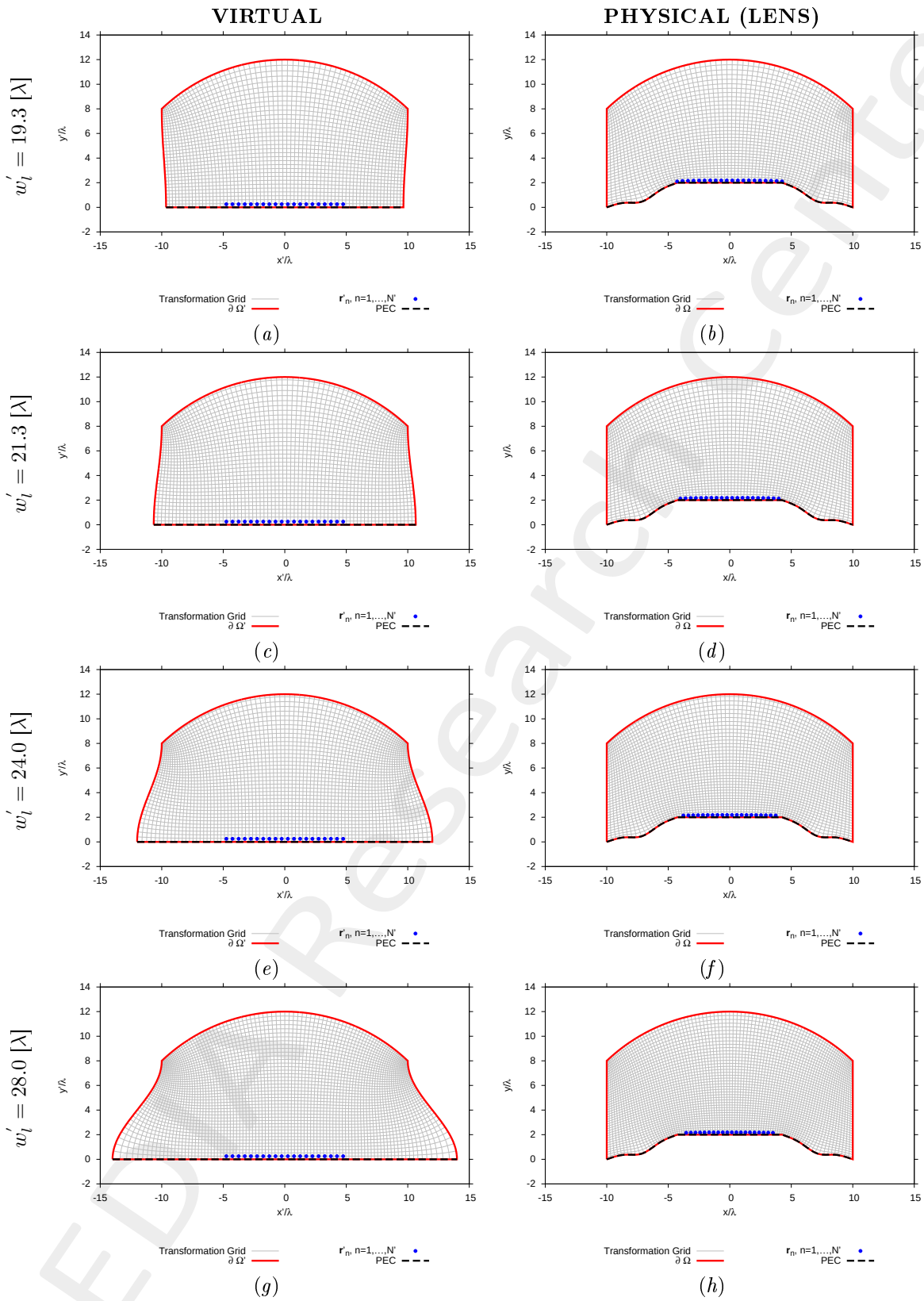

Figure 7: Transformation grids for virtual and physical geometries for different configurations of the lens.

Physical lens permittivity (Test case 1 - $w_l^{'} = 19.3\ [\lambda]$)

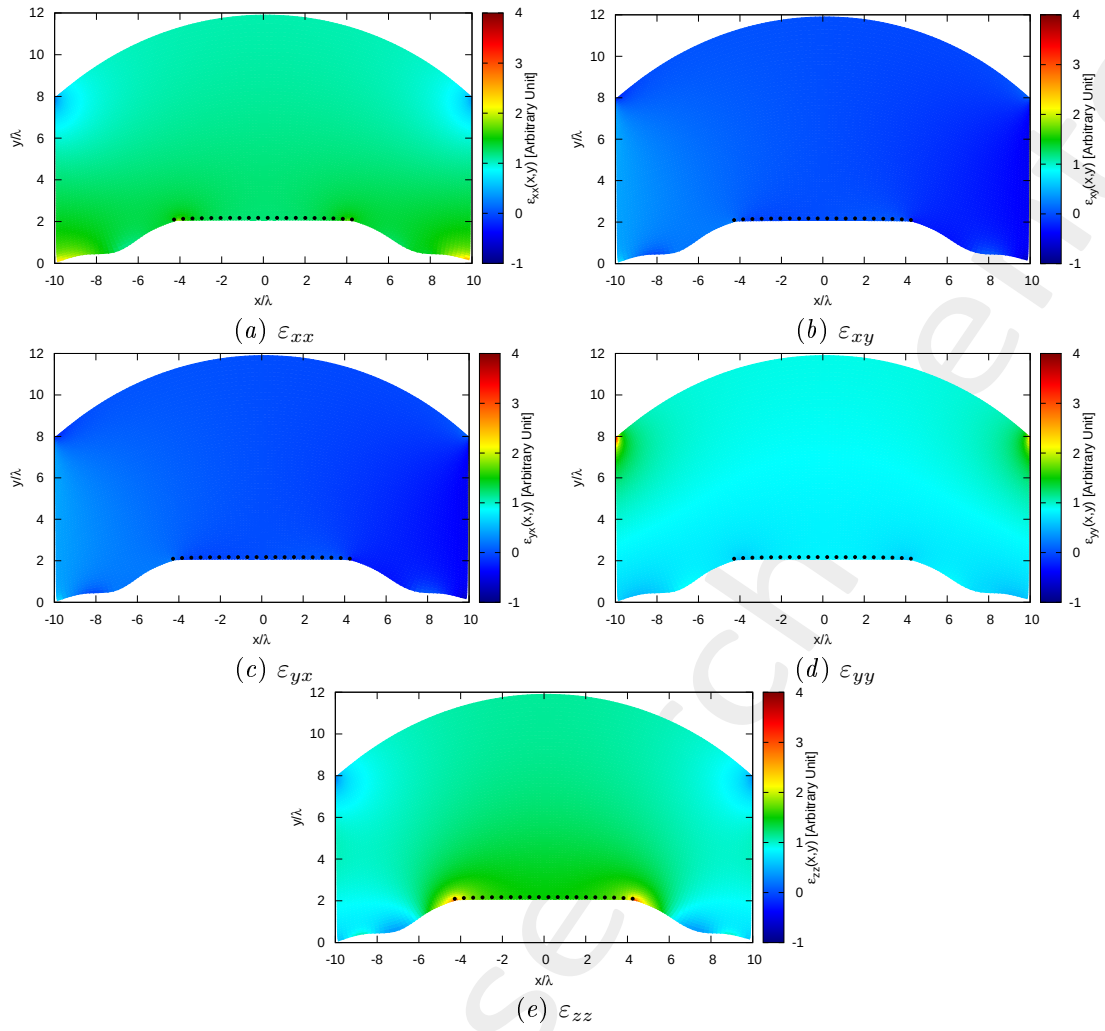

Figure 8: Components of the relative permittivity tensor of the lens.

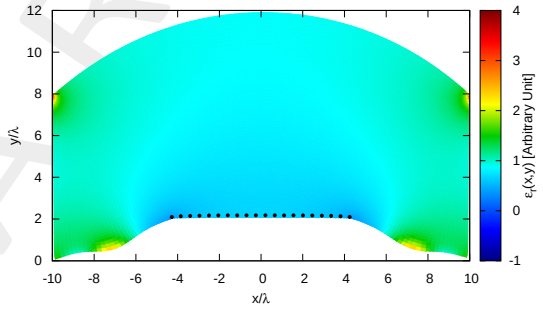

Figure 9: Isotropic approximate permittivity distribution of the lens.

Physical lens permittivity (Test case 2 - $w_l^{'} = 21.3\ [\lambda]$)

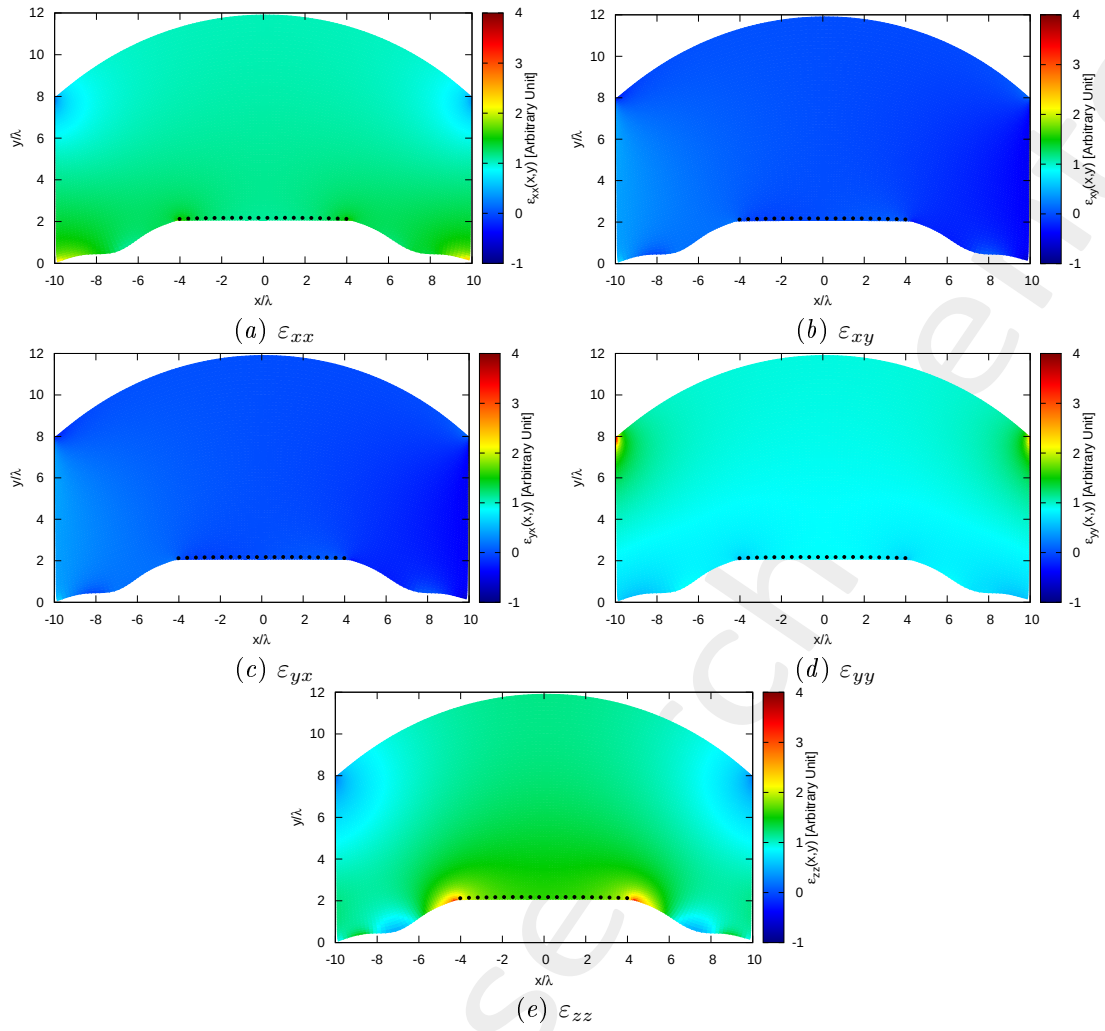

Figure 10: Components of the relative permittivity tensor of the lens.

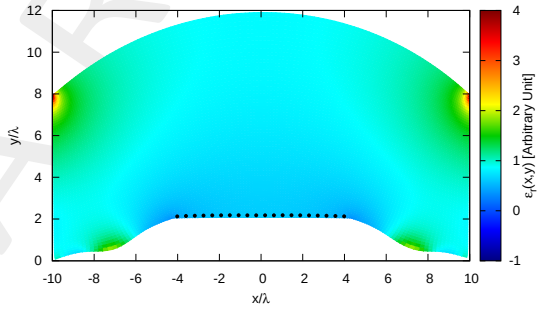

Figure 11: Isotropic approximate permittivity distribution of the lens.

Physical lens permittivity (Test case 3 - $w_l^{'} = 24.0$ [λ])

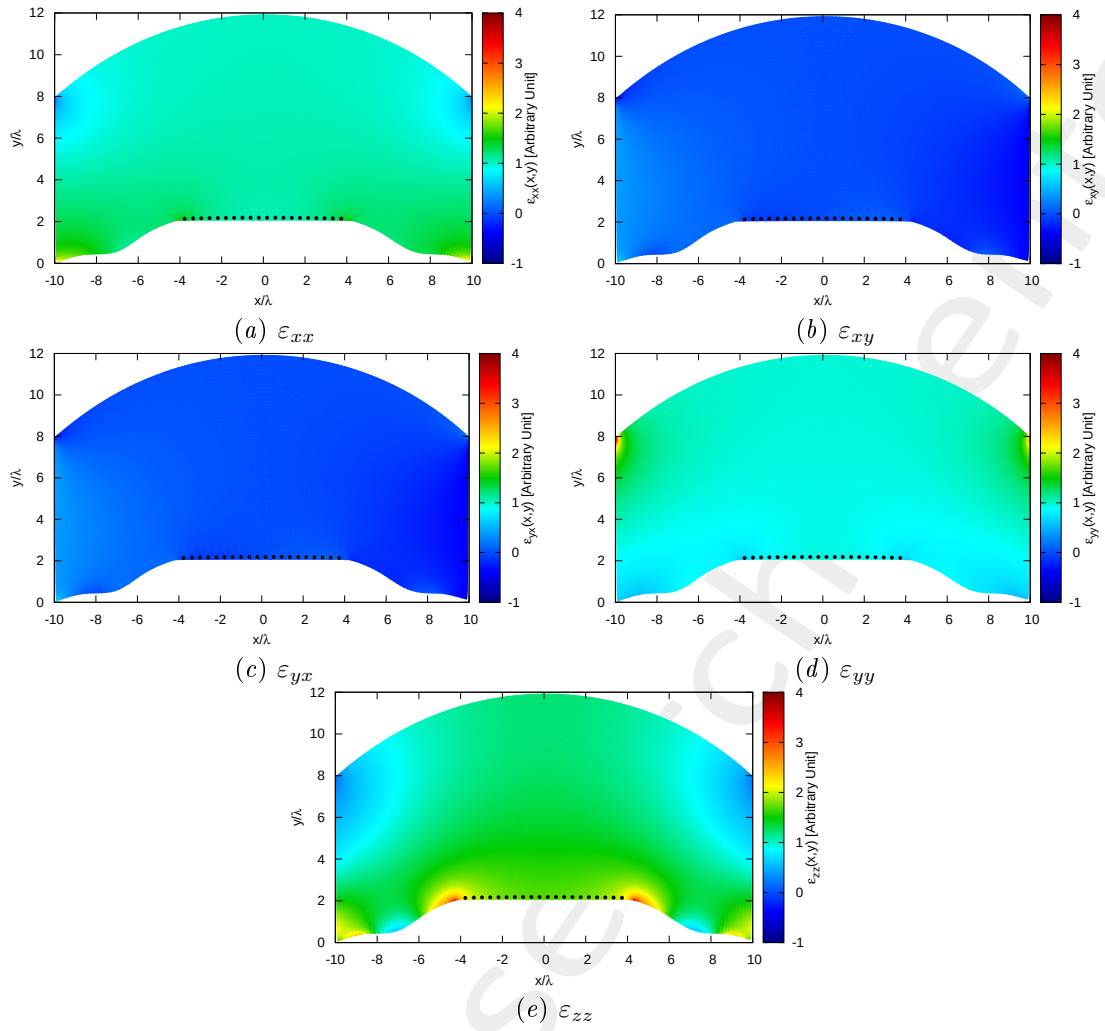

Figure 12: Components of the relative permittivity tensor of the lens.

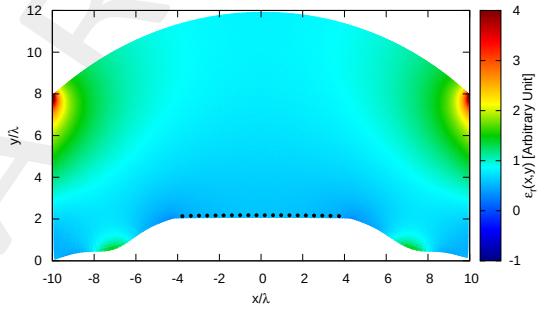

Figure 13: Isotropic approximate permittivity distribution of the lens.

Physical lens permittivity (Test case 4 - $w_l^{'} = 28.0$ [λ])

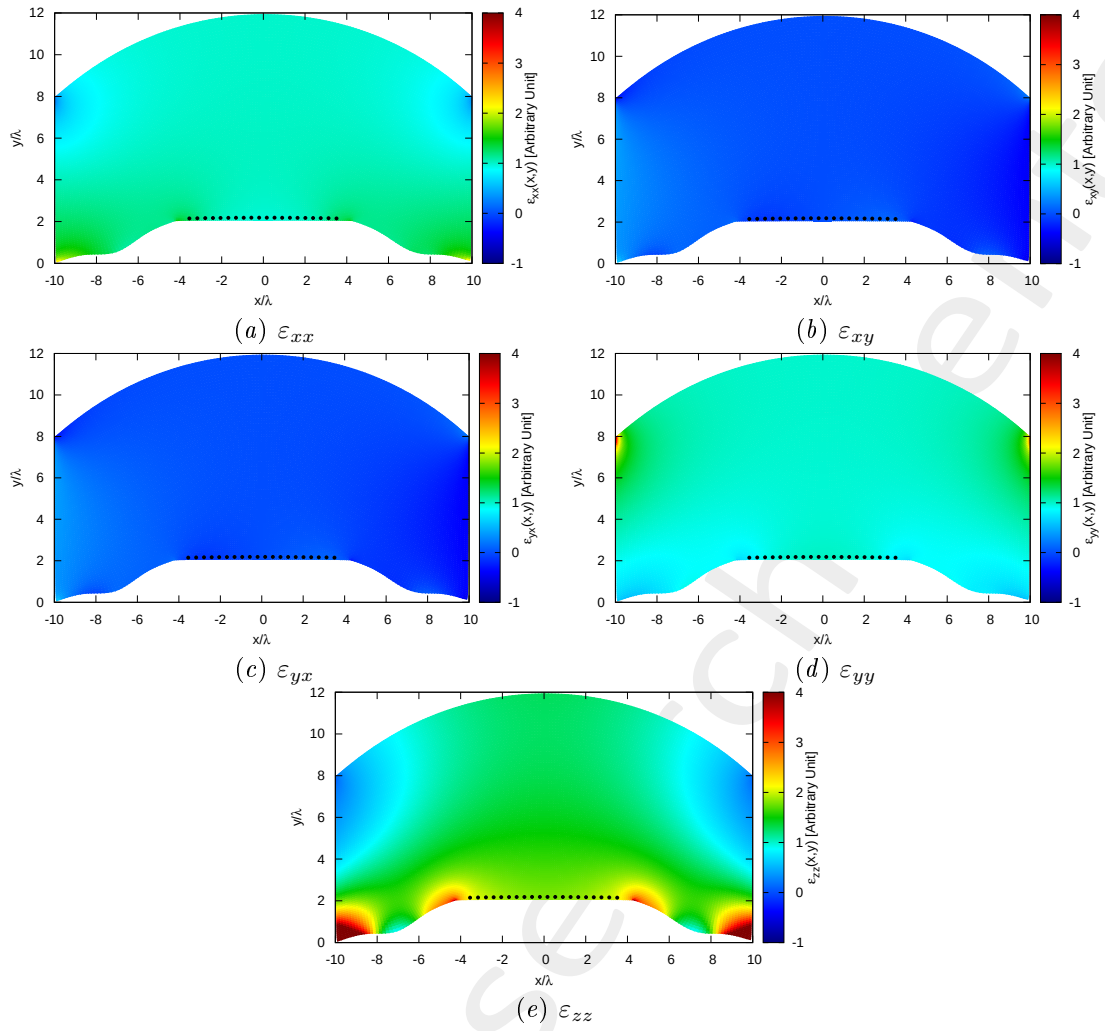

Figure 14: Components of the relative permittivity tensor of the lens.

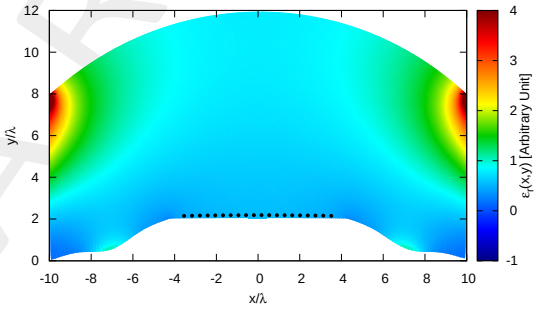

Figure 15: Isotropic approximate permittivity distribution of the lens.

2.0.7 Far-Field Patterns ($\phi_s = 90$ [deg], $f = 600$ [MHz], Aniso-Lens)

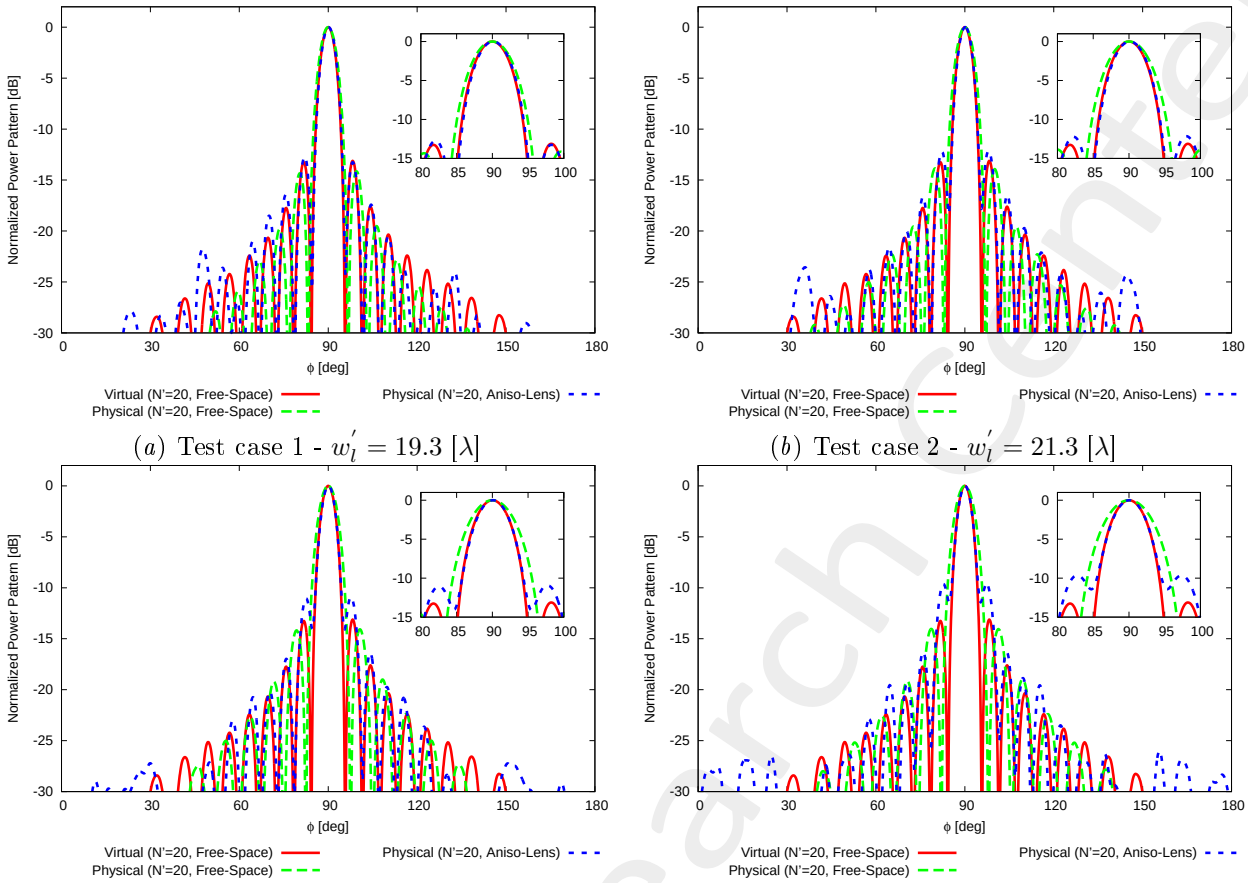

(a) Test case 1 - $w_l^{'} = 19.3$ [λ]

(b) Test case 2 - $w_l^{'} = 21.3$ [λ]

(c) Test case 3 - $w_l^{'} = 24.0$ [λ]

(d) Test case 4 - $w_l^{'} = 28.0$ [λ]

Figure 16: Comparison between the far field patterns of virtual and physical "dense" arrays.

2.1 Reduction of the Control Points through SI ($N' \rightarrow N < N'$)

Parameters

- Number of array elements before SI: $N' = 20$;
- Number of array elements after SI (N): check table below;
- Spacing after SI: $d = \lambda/2$;
- Radius of the observation domain: $r_{SI} = 400$ [λ];
- Number of field sampling points: $n_{SI} = 1000$.

	Before SI		**After SI**	
TEST CASE	N_{dense}	L_{dense} [λ]	N	L [λ]
1	20	8.52	18	8.50
2	20	8.00	17	8.00
3	20	7.50	16	7.50
4	20	7.05	15	7.00

Table VI: Parameters considered for SI.

2.1.1 Far-Field Patterns After SI ($\phi_s = 90$ [deg], $f = 600$ [MHz], Aniso-Lens)

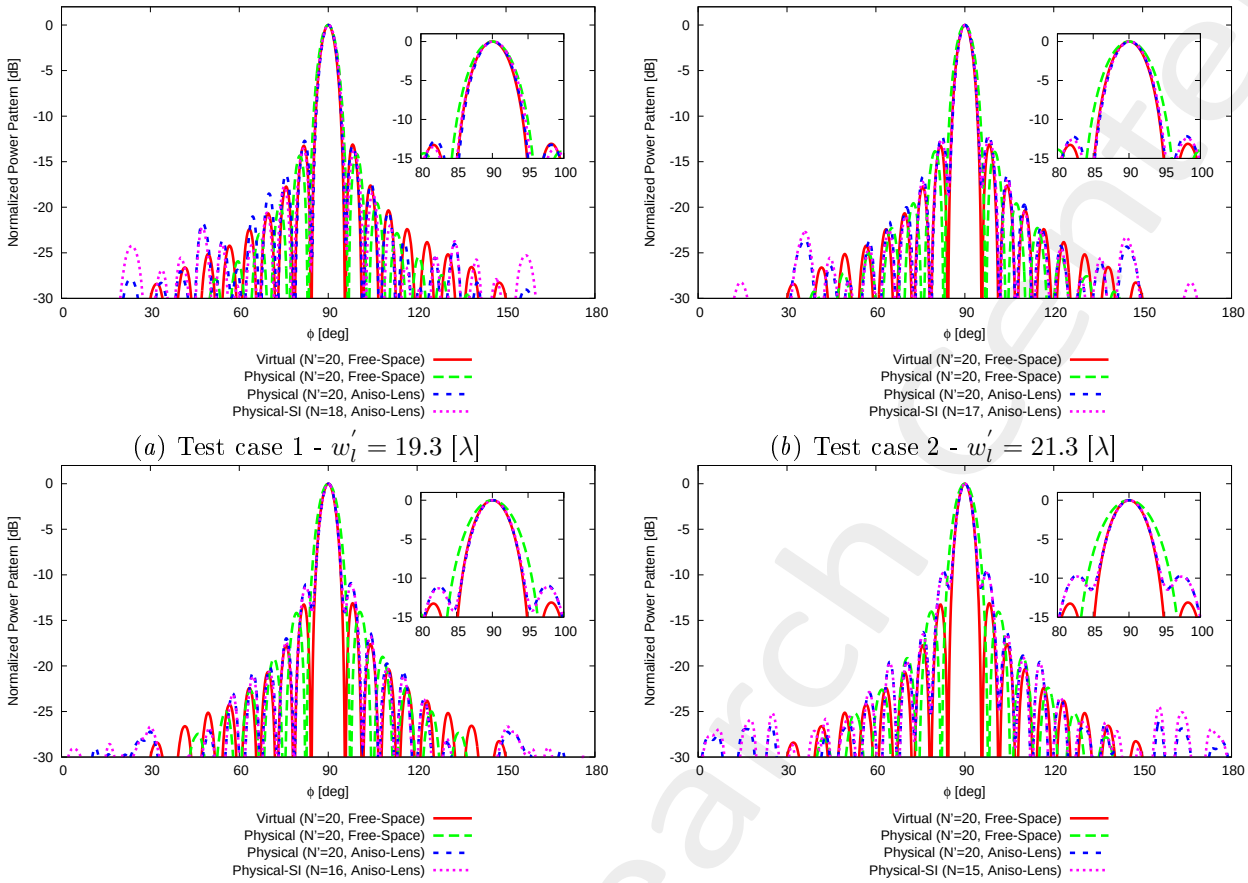

(a) Test case 1 - $w_l^{'} = 19.3$ [λ]

(b) Test case 2 - $w_l^{'} = 21.3$ [λ]

(c) Test case 3 - $w_l^{'} = 24.0$ [λ]

(d) Test case 4 - $w_l^{'} = 28.0$ [λ]

Figure 17: Comparison between the far field patterns of virtual and physical arrays before and after SI.

3 "Circular-Arc-Low-Spline" Geometry - $N' = 20$ (With Compression) #2

Input Parameters

- **Virtual & Physical Geometries**

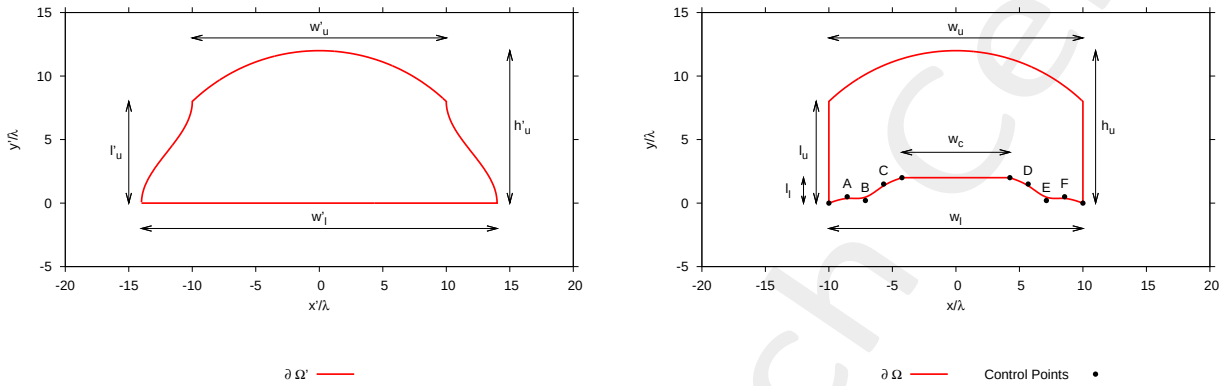

(*a*) **VIRTUAL** (*b*) **PHYSICAL (LENS)**

Figure 18: Transformation regions and geometric parameters of interest.

	VIRTUAL					PHYSICAL (LENS)												
TEST CASE	N'	w_l' [λ]	w_u' [λ]	h_u' [λ]	l_u' [λ]	N	w_l [λ]	w_u [λ]	h_u [λ]	l_u [λ]	l_l [λ]	w_c [λ]	y_A [λ]	y_B [λ]	y_C [λ]	y_D [λ]	y_E [λ]	y_F [λ]
1	20	**18.5**	20.0	11.0	8.0	**18**	20.0	20.0	11.0	8.0	3.0	8.5	1.5	0.0	2.0	2.0	0.0	1.5
2	20	**20.5**	20.0	11.0	8.0	**17**	20.0	20.0	11.0	8.0	3.0	8.5	1.5	0.0	2.0	2.0	0.0	1.5
3	20	**23.0**	20.0	11.0	8.0	**16**	20.0	20.0	11.0	8.0	3.0	8.5	1.5	0.0	2.0	2.0	0.0	1.5
4	20	**26.0**	20.0	11.0	8.0	**15**	20.0	20.0	11.0	8.0	3.0	8.5	1.5	0.0	2.0	2.0	0.0	1.5

Table VII: Executed test cases. Objective: increase w_l' in order to obtain larger compressions of the original virtual array.

IMPORTANT NOTE: The minimum compression is for $N = 18$ ($L = 8.5$ [λ]) because this is the length of the linear segment in the physical lens (i.e., $w_c = 8.5[\lambda]$) on which the compressed array must stay.

- **Virtual Array**
  - Number of elements, spacing, aperture: $N' = 20$, $d' = \frac{\lambda}{2}$, $L' = 9.5$ [λ];
  - Distance from PEC ground plane (placed at $y' = 0.0$): $\delta' = \frac{\lambda}{4}$;
  - Operating frequency: $f = 600$ [MHz];
  - Excitations for steering at $\phi = \phi_s$: $I_n = 1.0$, $\varphi_n = \frac{-2\pi}{\lambda} x_n sin\,(\phi_s + 90)$; $n = 1, ..., N'$;
- **QCTO**
  - Discretization cell dimension: 0.15 [λ] (0.01 [λ] for source mapping);

3.0.2 Results of the Transformation

Compression of the virtual array

	VIRTUAL			PHYSICAL (LENS)	
TEST CASE	N'	L' $[\lambda]$	$w_l^{'}$ $[\lambda]$	N_{dense}	$L_{dense}[\lambda]$
1	20	9.5	18.5	20	8.54
2	20	9.5	20.5	20	8.03
3	20	9.5	23.0	20	7.53
4	20	9.5	26.0	20	7.12

Table VIII: Number of elements and aperture of the array after compression from virtual to physical.

Physical lens parameters

	$w_l^{'} = 18.5$ $[\lambda]$	$w_l^{'} = 20.5$ $[\lambda]$	$w_l^{'} = 23.0$ $[\lambda]$	$w_l^{'} = 26.0$ $[\lambda]$
Anisotropic Permittivity Range	$[-5.41, 31.50]$	$[-4.62, 13.33]$	$[-4.44, 16.72]$	$[-4.30, 22.35]$
Isotropic Permittivity Range	$[0.00, 8.20]$	$[0.00, 6.58]$	$[0.00, 5.00]$	$[0.00, 5.42]$
Average Fractional Anisotropy, α_F	3.44×10^{-1}	3.26×10^{-1}	3.20×10^{-1}	3.25×10^{-1}
Average Relative Anisotropy, α_R	3.28×10^{-1}	3.10×10^{-1}	3.06×10^{-1}	3.17×10^{-1}

Table IX: Permittivity ranges and anisotropy measures of the physical lens.

Transformation grids

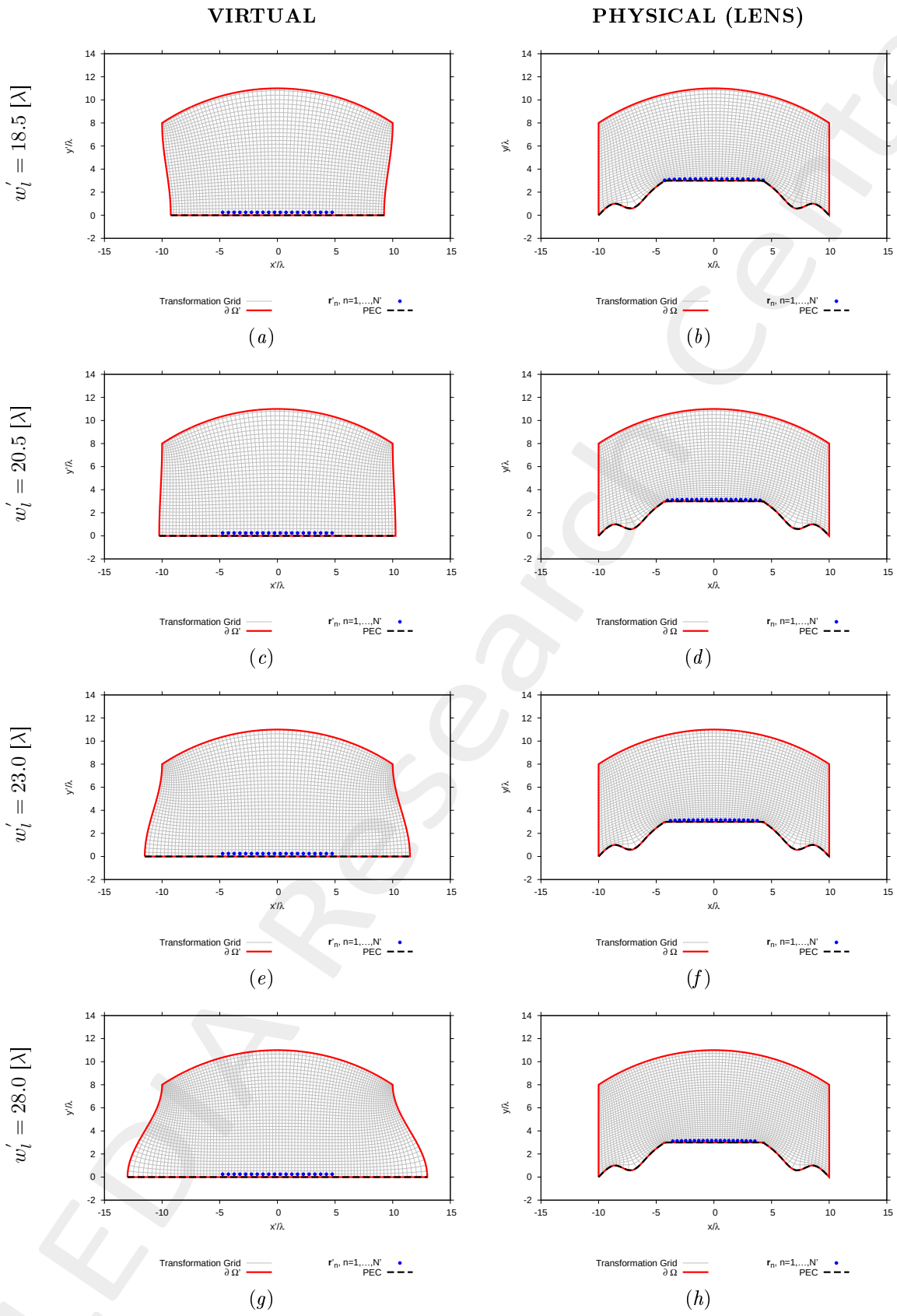

Figure 19: Transformation grids for virtual and physical geometries for different configurations of the lens.

Physical lens permittivity (Test case 1 - $w_l^{'} = 18.5$ [λ])

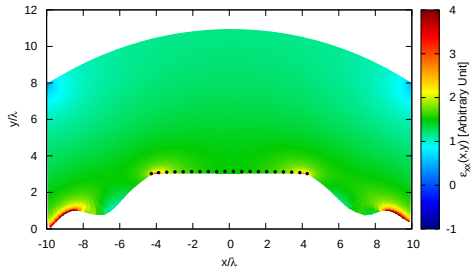

(a) ε_{xx}

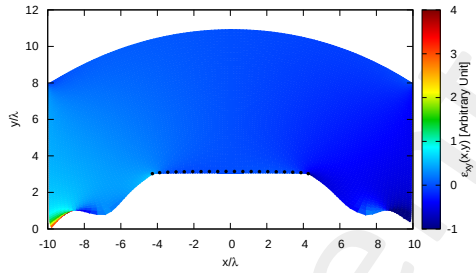

(b) ε_{xy}

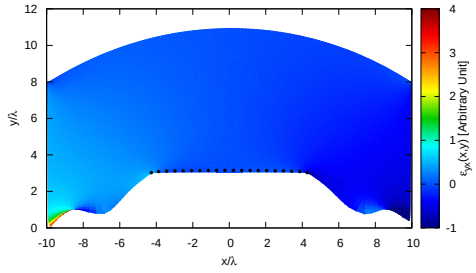

(c) ε_{yx}

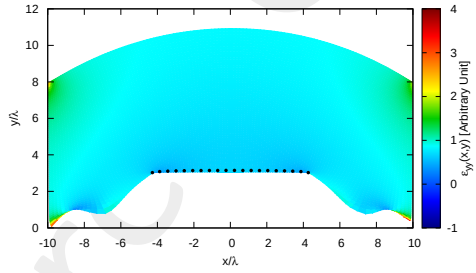

(d) ε_{yy}

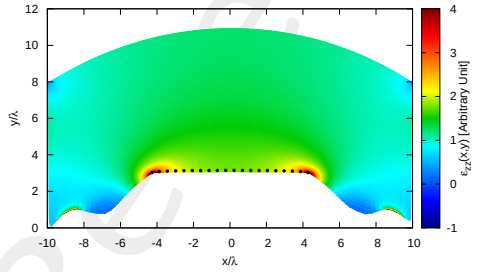

(e) ε_{zz}

Figure 20: Components of the relative permittivity tensor of the lens.

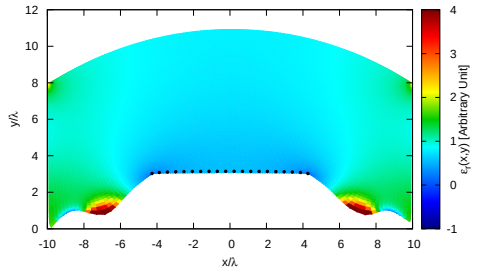

Figure 21: Isotropic approximate permittivity distribution of the lens.

Physical lens permittivity (Test case 2 - $w_l^{'} = 20.5$ [λ])

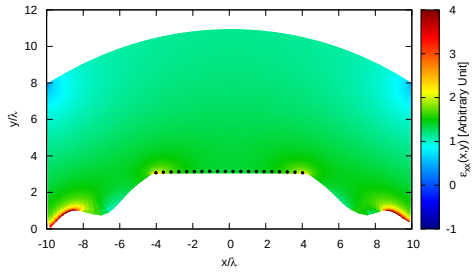

(a) ε_{xx}

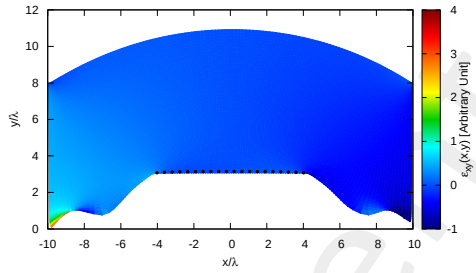

(b) ε_{xy}

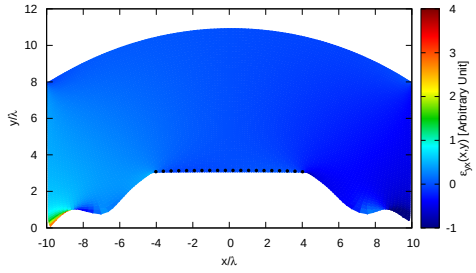

(c) ε_{yx}

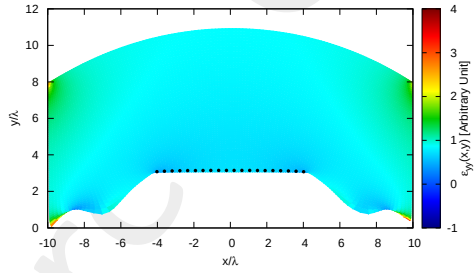

(d) ε_{yy}

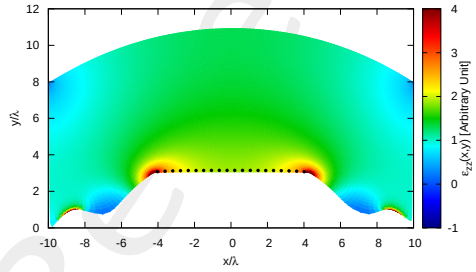

(e) ε_{zz}

Figure 22: Components of the relative permittivity tensor of the lens.

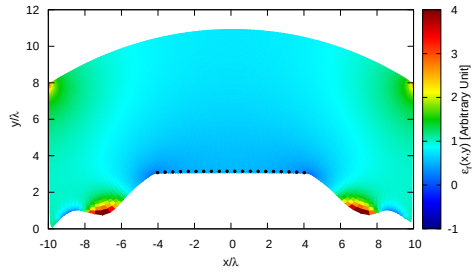

Figure 23: Isotropic approximate permittivity distribution of the lens.

Physical lens permittivity (Test case 3 - $w_l^{'} = 23.0$ [λ])

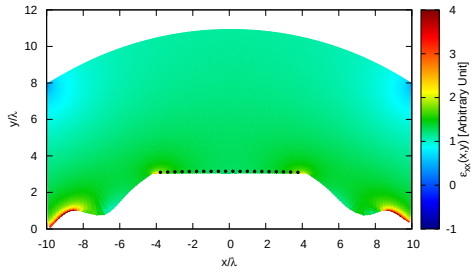

(a) ε_{xx}

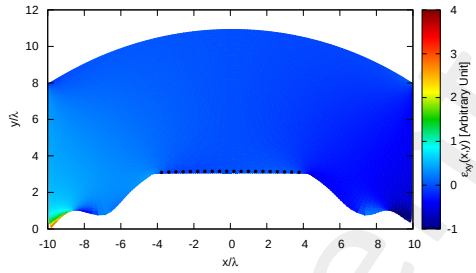

(b) ε_{xy}

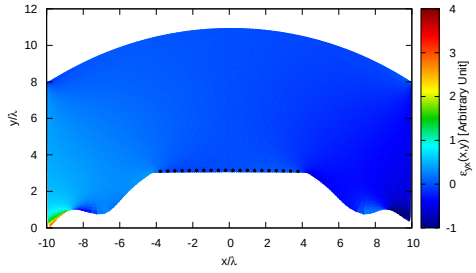

(c) ε_{yx}

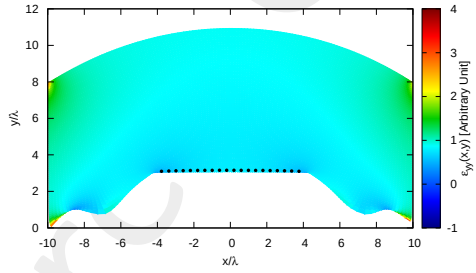

(d) ε_{yy}

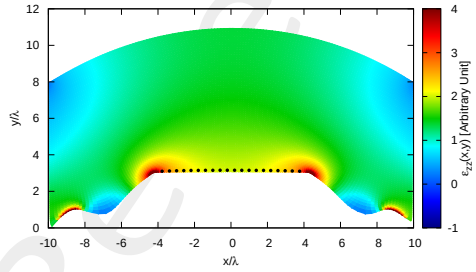

(e) ε_{zz}

Figure 24: Components of the relative permittivity tensor of the lens.

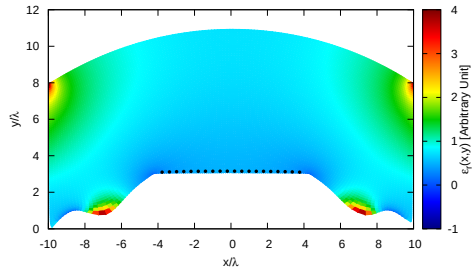

Figure 25: Isotropic approximate permittivity distribution of the lens.

Physical lens permittivity (Test case 4 - $w_l^{'} = 26.0$ [λ])

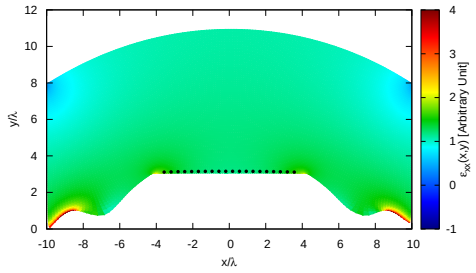

(a) ε_{xx}

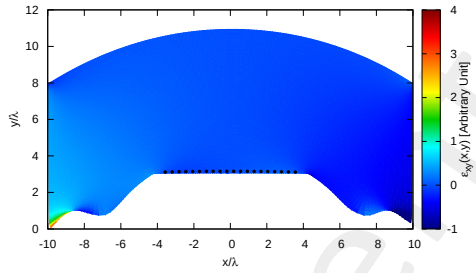

(b) ε_{xy}

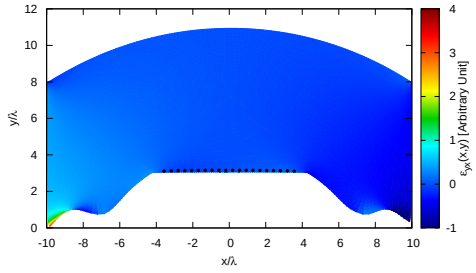

(c) ε_{yx}

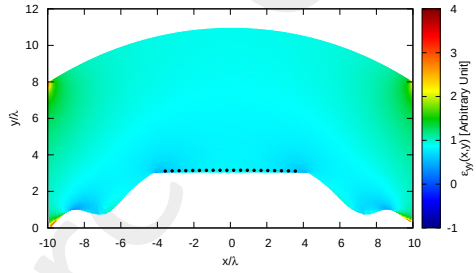

(d) ε_{yy}

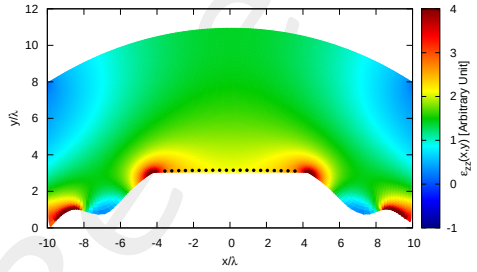

(e) ε_{zz}

Figure 26: Components of the relative permittivity tensor of the lens.

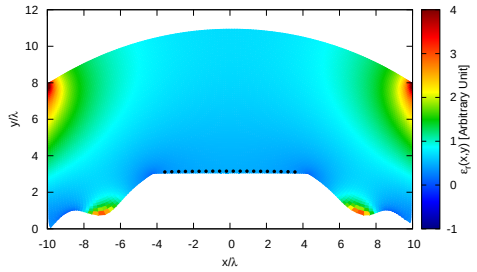

Figure 27: Isotropic approximate permittivity distribution of the lens.

3.0.3 Far-Field Patterns ($\phi_s = 90$ [deg], $f = 600$ [MHz], Aniso-Lens)

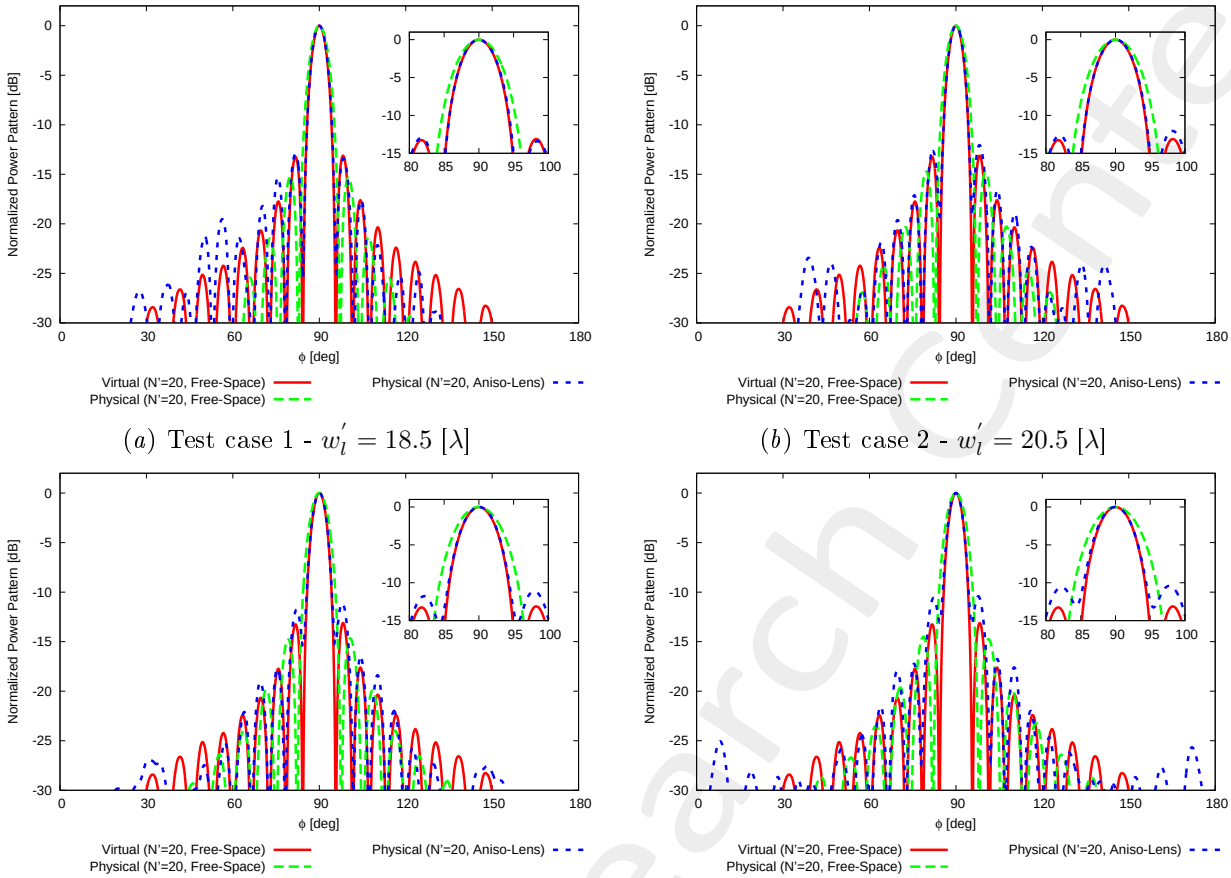

(a) Test case 1 - $w_l^{'} = 18.5$ [λ]

(b) Test case 2 - $w_l^{'} = 20.5$ [λ]

(c) Test case 3 - $w_l^{'} = 23.0$ [λ]

(d) Test case 4 - $w_l^{'} = 26.0$ [λ]

Figure 28: Comparison between the far field patterns of virtual and physical "dense" arrays.

3.1 Reduction of the Control Points through SI ($N' \rightarrow N < N'$)

Parameters

- Number of array elements before SI: $N' = 20$;
- Number of array elements after SI (N): check table below;
- Spacing after SI: $d = \lambda/2$;
- Radius of the observation domain: $r_{SI} = 400$ [λ];
- Number of field sampling points: $n_{SI} = 1000$.

	Before SI		**After SI**	
TEST CASE	N_{dense}	L_{dense} [λ]	N	L [λ]
1	20	8.54	18	8.50
2	20	8.03	17	8.00
3	20	7.53	16	7.50
4	20	7.12	15	7.00

Table X: Parameters considered for SI.

3.1.1 Far-Field Patterns After SI ($\phi_s = 90$ [deg], $f = 600$ [MHz], Aniso-Lens)

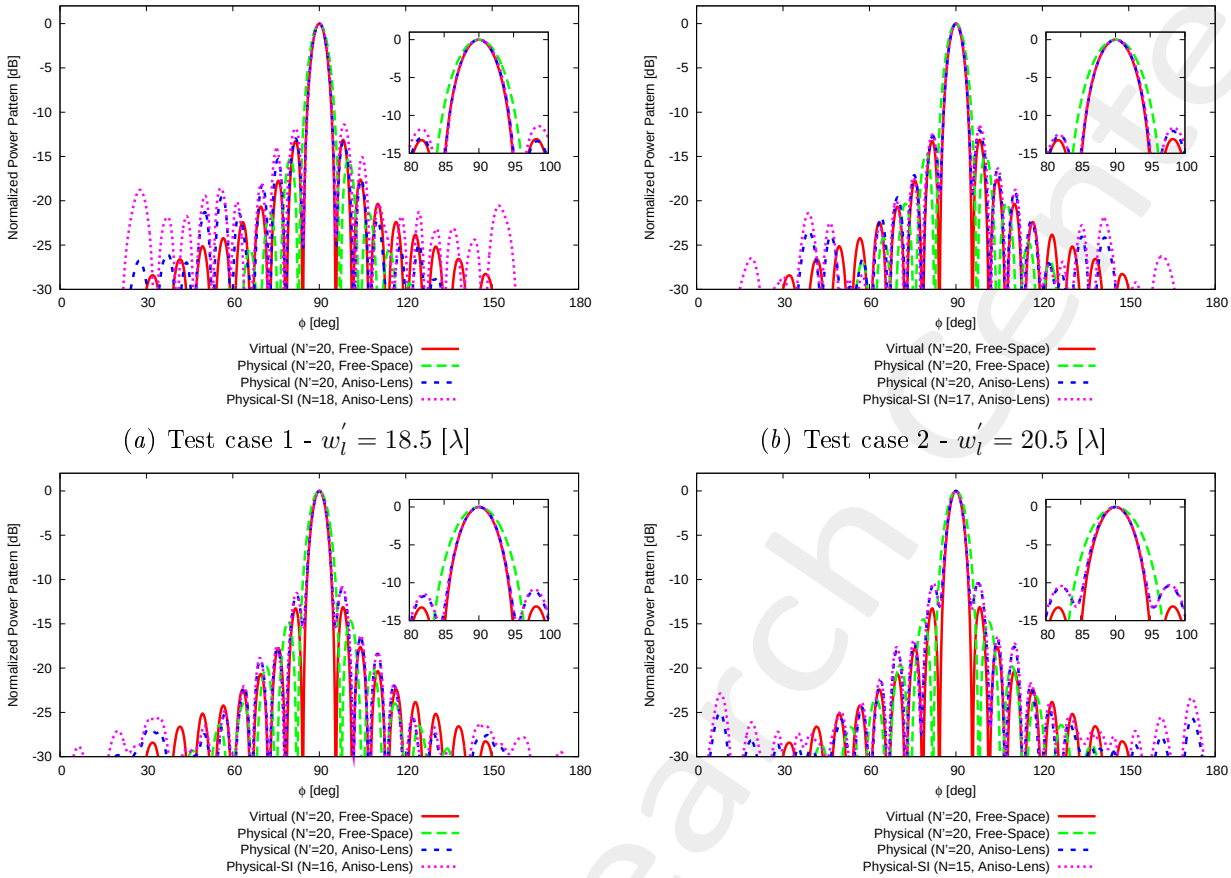

(a) Test case 1 - $w_l^{'} = 18.5$ [λ]

(b) Test case 2 - $w_l^{'} = 20.5$ [λ]

(c) Test case 3 - $w_l^{'} = 23.0$ [λ]

(d) Test case 4 - $w_l^{'} = 26.0$ [λ]

Figure 29: Comparison between the far field patterns of virtual and physical arrays before and after SI.

References

[1] G. Oliveri, G. Gottardi, F. Robol, A. Polo, L. Poli, M. Salucci, M. Chuan, C. Massagrande, P. Vinetti, M. Mattivi, R. Lombardi, and A. Massa, "Co-design of unconventional array architectures and antenna elements for 5G base station," *IEEE Trans. Antennas Propag.*, vol. 65, no. 12, pp. 6752-6767, Dec. 2017.

[2] P. Rocca, G. Oliveri, R. J. Mailloux, and A. Massa, "Unconventional phased array architectures and design methodologies - A review," *Proc. IEEE*, vol. 104, no. 3, pp. 544-560, Mar. 2016.

[3] G. Oliveri, M. Salucci, N. Anselmi and A. Massa, "Multiscale System-by-Design synthesis of printed WAIMs for waveguide array enhancement," *IEEE J. Multiscale Multiphysics Computat. Techn.*, vol. 2, pp. 84-96, 2017.

[4] A. Massa and G. Oliveri, "Metamaterial-by-Design: Theory, methods, and applications to communications and sensing - Editorial," *EPJ Applied Metamaterials*, vol. 3, no. E1, pp. 1-3, 2016.

[5] L. Poli, G. Oliveri, P. Rocca, M. Salucci, and A. Massa, "Long-Distance WPT Unconventional Arrays Synthesis," *J. Electromagnet. Waves Appl.*, vol. 31, no. 14, pp. 1399-1420, Jul. 2017.

[6] G. Oliveri, F. Viani, N. Anselmi, and A. Massa, "Synthesis of multi-layer WAIM coatings for planar phased arrays within the system-by-design framework," *IEEE Trans. Antennas Propag.*, vol. 63, no. 6, pp. 2482-2496, Jun. 2015.

[7] G. Oliveri, L. Tenuti, E. Bekele, M. Carlin, and A. Massa, "An SbD-QCTO approach to the synthesis of isotropic metamaterial lenses," *IEEE Antennas Wireless Propag. Lett.*, vol. 13, pp. 1783-1786, 2014.

[8] G. Oliveri, D. H. Werner, and A. Massa, "Reconfigurable electromagnetics through metamaterials - A review" *Proc. IEEE*, vol. 103, no. 7, pp. 1034-1056, Jul. 2015.

[9] G. Oliveri, E. T. Bekele, M. Salucci, and A. Massa, "Transformation electromagnetics miniaturization of sectoral and conical horn antennas," *IEEE Trans. Antennas Propag.*, vol. 64, no. 4, pp. 1508-1513, Apr. 2016.

[10] G. Oliveri, E. T. Bekele, M. Salucci, and A. Massa, "Array miniaturization through QCTO-SI metamaterial radomes," *IEEE Trans. Antennas Propag.*, vol. 63, no. 8, pp. 3465-3476, Aug. 2015.

[11] G. Oliveri, E. T. Bekele, D. H. Werner, J. P. Turpin, and A. Massa, "Generalized QCTO for metamaterial-lens-coated conformal arrays," *IEEE Trans. Antennas Propag.*, vol. 62, no. 8, pp 4089-4095, Aug. 2014.

[12] G. Oliveri, E. Bekele, M. Carlin, L. Tenuti, J. Turpin, D. H. Werner, and A. Massa, "Extended QCTO for innovative antenna system designs," IEEE Antenna Conference on Antenna Measurements and Applications (CAMA 2014), pp. 1-3, Nov. 16-19, 2014.

[13] G. Oliveri, P. Rocca, M. Salucci, E. T. Bekele, D. H. Werner, and A. Massa, "Design and synthesis of innovative metamaterial-enhanced arrays," IEEE International Symposium on Antennas Propag. (APS/URSI 2013), Orlando, Florida, USA, pp. 972 - 973, Jul. 7-12, 2013.

[14] G. Oliveri, "Improving the reliability of frequency domain simulators in the presence of homogeneous metamaterials - A preliminary numerical assessment," *Progress In Electromagnetics Research*, vol. 122, pp. 497-518, 2012.

[15] M. Salucci, G. Oliveri, N. Anselmi, G. Gottardi, and A. Massa, "Performance enhancement of linear active electronically-scanned arrays by means of MbD-synthesized metalenses," *J. Electromagnet. Waves Appl.*, vol. 32, no. 8, pp. 927-955, 2018.

[16] M. Salucci, G. Oliveri, N. Anselmi, and A. Massa, "Material-by-design synthesis of conformal miniaturized linear phased arrays," *IEEE Access* (doi: 10.1109/ACCESS.2018.2833199).